

# Geophysical Research Letters<sup>®</sup>



## RESEARCH LETTER

10.1029/2025GL116473

## Interplay Between a Foreshock Bubble and a Hot Flow Anomaly Forming Along the Same Rotational Discontinuity

### Key Points:

- A single directional magnetic field discontinuity can generate several types of foreshock transients
- Foreshock bubbles can modify their driving discontinuity and create favorable conditions for the formation of hot flow anomalies
- Bow shock deformation and erosion are caused by changes in the upstream solar wind parameters within the foreshock transient

Lucile Turc<sup>1</sup> , Martin O. Archer<sup>2</sup> , Hongyang Zhou<sup>3</sup>, Yann Pfau-Kempf<sup>4</sup> , Jonas Suni<sup>1</sup> , Primož Kajdič<sup>5</sup> , Xóchitl Blanco-Cano<sup>5</sup> , Souhail Dahani<sup>1</sup> , Markus Battarbee<sup>1</sup> , Savvas Raptis<sup>6</sup> , Terry Z. Liu<sup>7</sup> , Hui Zhang<sup>8</sup> , C. Philippe Escoubet<sup>9</sup> , Adrian T. LaMoury<sup>2</sup> , Shi Tao<sup>1</sup> , Veera Lipsanen<sup>1</sup>, Yufei Hao<sup>10</sup> , and Minna Palmroth<sup>1,11</sup> 

<sup>1</sup>Department of Physics, University of Helsinki, Helsinki, Finland, <sup>2</sup>The Blackett Laboratory, Imperial College London, South Kensington, UK, <sup>3</sup>Center for Space Physics, Boston University, Boston, MA, USA, <sup>4</sup>CSC-IT Center for Science, Espoo, Finland, <sup>5</sup>Space Science Department, Geophysics Institute, Universidad Nacional Autónoma de México, Mexico City, Mexico, <sup>6</sup>Johns Hopkins University Applied Physics Laboratory, Laurel, MD, USA, <sup>7</sup>Department of Earth, Planetary, and Space Sciences, University of California, Los Angeles, CA, USA, <sup>8</sup>School of Space Science and Technology, Shandong University, Weihai, China, <sup>9</sup>ESA/ESTEC, Noordwijk, The Netherlands, <sup>10</sup>Key Laboratory of Planetary Sciences, Chinese Academy of Sciences, Purple Mountain Observatory, Nanjing, China, <sup>11</sup>Space and Earth Observation Centre, Finnish Meteorological Institute, Helsinki, Finland

### Correspondence to:

L. Turc,  
lucile.turc@helsinki.fi

### Citation:

Turc, L., Archer, M. O., Zhou, H., Pfau-Kempf, Y., Suni, J., Kajdič, P., et al. (2025). Interplay between a foreshock bubble and a hot flow anomaly forming along the same rotational discontinuity. *Geophysical Research Letters*, 52, e2025GL116473. <https://doi.org/10.1029/2025GL116473>

Received 10 APR 2025  
Accepted 28 MAY 2025

### Author Contributions:

**Conceptualization:** Lucile Turc, Martin O. Archer  
**Data curation:** Hongyang Zhou, Yann Pfau-Kempf, Jonas Suni  
**Formal analysis:** Lucile Turc, Martin O. Archer, Souhail Dahani, Markus Battarbee  
**Funding acquisition:** Lucile Turc, Primož Kajdič, Xóchitl Blanco-Cano, Minna Palmroth  
**Investigation:** Lucile Turc, Hongyang Zhou, Yann Pfau-Kempf, Jonas Suni  
**Methodology:** Lucile Turc, Markus Battarbee  
**Project administration:** Lucile Turc, Primož Kajdič, Xóchitl Blanco-Cano  
**Resources:** Lucile Turc  
**Software:** Hongyang Zhou, Yann Pfau-Kempf, Jonas Suni, Markus Battarbee  
**Supervision:** Lucile Turc

**Abstract** Solar wind directional discontinuities can generate transient mesoscale structures such as foreshock bubbles and hot flow anomalies (HFAs) upstream of Earth's bow shock. These structures can have a global impact on near-Earth space, so understanding their formation conditions is essential. We investigate foreshock transient generation at a rotational discontinuity using a global 2D hybrid-Vlasov simulation. As expected, a foreshock bubble forms on the sunward side of the discontinuity. Later, when the discontinuity reaches the shock, new structures identified as HFAs develop, despite the initial discontinuity not being favorable to HFA formation. We demonstrate that the foreshock bubble provides the necessary conditions for their generation. We then investigate the evolution of the transient structures and the large-scale bow shock deformation they induce. Our results provide new insights on the formation and evolution of foreshock transients and their impact on the shock.

**Plain Language Summary** Earth's magnetic field extends into space and forms a magnetic shield, the magnetosphere, which protects our planet from particles originating from the Sun. This stream of particles, the solar wind, carries with it the solar magnetic field and fills the entire solar system. Abrupt turns in the solar magnetic field can lead to particles accumulating in a small region of space, creating transient structures which rapidly grow, in a few minutes, to sizes comparable to Earth or even larger. When they impact Earth's magnetosphere, these structures cause disturbances such as oscillations of the Earth's magnetic field lines or brightening of the aurora. Here, we use a supercomputer model to better understand how these structures are formed. We show that several of them can grow when a single solar wind magnetic field turning reaches near-Earth space because the first structure modifies its environment, enabling more particles to accumulate. As they travel toward Earth, these structures reach the bow shock, which slows down the solar wind before it hits the magnetosphere. The part of the shock impacted by the structures deforms and weakens.

## 1. Introduction

Foreshock transients are mesoscale structures, with sizes ranging from a few ion inertial lengths to over ten planetary radii, generated by ion kinetic processes upstream of collisionless shocks (Zhang et al., 2022). They have been observed at shocks throughout the solar system (Omidi, Collinson, & Sibeck, 2020; Valek et al., 2017; Zhang et al., 2022), and play an important role in particle acceleration (Liu et al., 2019; Raptis et al., 2025; Turner et al., 2018; Wilson et al., 2016). At Earth, foreshock transients also significantly disturb the magnetosphere (Kajdič et al., 2024). Uncovering the formation mechanisms of foreshock transients is therefore crucial to understand both the dynamics of collisionless shocks and their impact on near-Earth space.

Some foreshock transients are generated spontaneously in the ion foreshock, the region extending upstream of the quasi-parallel bow shock and populated with backstreaming suprathermal particles (Blanco-Cano et al., 2009; Eastwood et al., 2005; Wilson, 2016; Zhang et al., 2022). The largest structures, foreshock bubbles and hot flow

© 2025. The Author(s).

This is an open access article under the terms of the [Creative Commons Attribution License](https://creativecommons.org/licenses/by/4.0/), which permits use, distribution and reproduction in any medium, provided the original work is properly cited.

**Validation:** Lucile Turc, Hongyang Zhou, Yann Pfau-Kempf, Jonas Suni

**Visualization:** Lucile Turc

**Writing – original draft:** Lucile Turc

**Writing – review & editing:** Lucile Turc,

Martin O. Archer, Hongyang Zhou,

Yann Pfau-Kempf, Jonas Suni,

Primož Kajdič, Xóchitl Blanco-Cano,

Souhail Dahani, Markus Battarbee,

Savvas Raptis, Terry Z. Liu, Hui Zhang,

C. Philippe Escoubet, Adrian T. LaMoury,

Shi Tao, Veera Lipsanen, Yufei Hao,

Minna Palmroth

anomalies (HFAs), are however due to suprathermal ion concentration at solar wind directional discontinuities (Omidi et al., 2010; Schwartz et al., 1985; Zhang et al., 2022). Hot flow anomalies form when the discontinuity intersects the bow shock and the convection electric field points toward the discontinuity on at least one side, channeling suprathermal ions into the structure (Schwartz, 1995; Zhao et al., 2017). In contrast, foreshock bubbles grow while the discontinuity travels through the foreshock, and there is no requirement on the motional electric field orientation (Archer et al., 2015; Omidi et al., 2010; Turner et al., 2013). The change in magnetic field direction across the discontinuity enables foreshock ions to accumulate on its sunward side. Both types of structures are characterized by a low density core filled with hot plasma, where the solar wind is significantly deflected. The expansion of this core results in the formation of a compression region, on the sunward side only for foreshock bubbles, and on one or both sides for HFAs. If the expansion is faster than the fast-magnetosonic speed, this compressed edge becomes a shock (Zhang et al., 2022).

It was initially thought that foreshock bubbles were driven solely by rotational discontinuities (Turner et al., 2013), while HFAs were associated with tangential discontinuities (Schwartz et al., 2000). Observations have now revealed that foreshock bubbles can be formed by both types of discontinuities (Liu et al., 2015), and this has been confirmed by simulations (Vu et al., 2022; Wang et al., 2021). As for HFAs, there is to our knowledge only one observational report of such a structure associated with a rotational discontinuity (Liu et al., 2016). Furthermore, numerical simulations by Omidi, Lee, et al. (2020) and Omidi, Collinson, and Sibeck (2020) indicate that both a foreshock bubble and an HFA can be created along the same rotational discontinuity as it interacts with the shock and the foreshock. These works did not however explore the physical mechanisms responsible for HFA formation.

We use the Vlasiator model (Palmroth et al., 2018) to study the formation of foreshock transients. Vlasiator has been extensively used to study foreshock processes, such as foreshock waves (Palmroth et al., 2015; Turc et al., 2018, 2019, 2023) and spontaneous foreshock transients (Blanco-Cano et al., 2018; Tarvus et al., 2021). Here, an earthward-propagating rotational discontinuity is injected into the two-dimensional (2D) simulation domain. As expected, the interaction of the discontinuity with foreshock ions creates a foreshock bubble. Still, we show that the same discontinuity also generates an HFA as it sweeps along the quasi-parallel bow shock. We demonstrate that the HFA formation is made possible by the foreshock bubble, and we investigate the evolution of both structures and their impact on the shock.

## 2. Simulation Model and Run Description

The Vlasiator model is based on a hybrid-Vlasov approach, in which ions are described as velocity distribution functions, while electrons are a massless, charge-neutralizing fluid (Ganse et al., 2023; Palmroth et al., 2018). Vlasov's equation, coupled with Maxwell's equations, is solved to determine the ion dynamics. Closure is provided by the generalized Ohm's law, including the Hall and the electron pressure gradient terms, assuming adiabatic electrons with a polytropic index of 5/3.

Here, we analyze a run with 2D in ordinary space, covering the equatorial plane of near-Earth space, and 3D in velocity space. The simulation domain extends from  $-10 R_E$  to  $30 R_E$  along the Sun-Earth line ( $x$ -axis) and  $\pm 40 R_E$  in the dawn-dusk direction ( $y$ -axis). All vector quantities are given in the Geocentric Solar Ecliptic coordinate system. The spatial resolution is 300 km in ordinary space and 31 km/s in velocity space. The simulation is initialized with steady solar wind parameters, density  $n_{SW} = 1 \text{ cm}^{-3}$ , velocity  $\mathbf{V}_{SW} = [-750, 0, 0] \text{ km/s}$ , temperature  $T_{SW} = 0.5 \text{ MK}$ , and magnetic field  $\mathbf{B} = [2.12, 2.12, 0] \text{ nT}$ . This corresponds to an upstream ion inertial length of 228 km and a thermal most probable proton energy of 43 eV, that is, hot and fast solar wind conditions. As demonstrated by Pfau-Kempf et al. (2018), the chosen resolution in both ordinary and velocity space is sufficient for ion kinetic processes to emerge due to the employed hybrid-Vlasov scheme, resulting in realistic ion foreshock properties.

After 300 s, during which the near-Earth system forms self-consistently, we inject a rotational discontinuity at the  $+x$  boundary of the simulation domain, changing the magnetic field orientation to  $\mathbf{B}_2 = [2.12, -2.12, 0] \text{ nT}$  and the velocity to  $\mathbf{V}_2 = [-750, -103, 0] \text{ km/s}$ . The changes in velocity and magnetic field across the discontinuity are chosen so that they approximately satisfy the Walén relation, based on magnetohydrodynamic (MHD) theory for rotational discontinuities (Lin, 1997). The discontinuity is planar with its normal along the Sun-Earth line. The

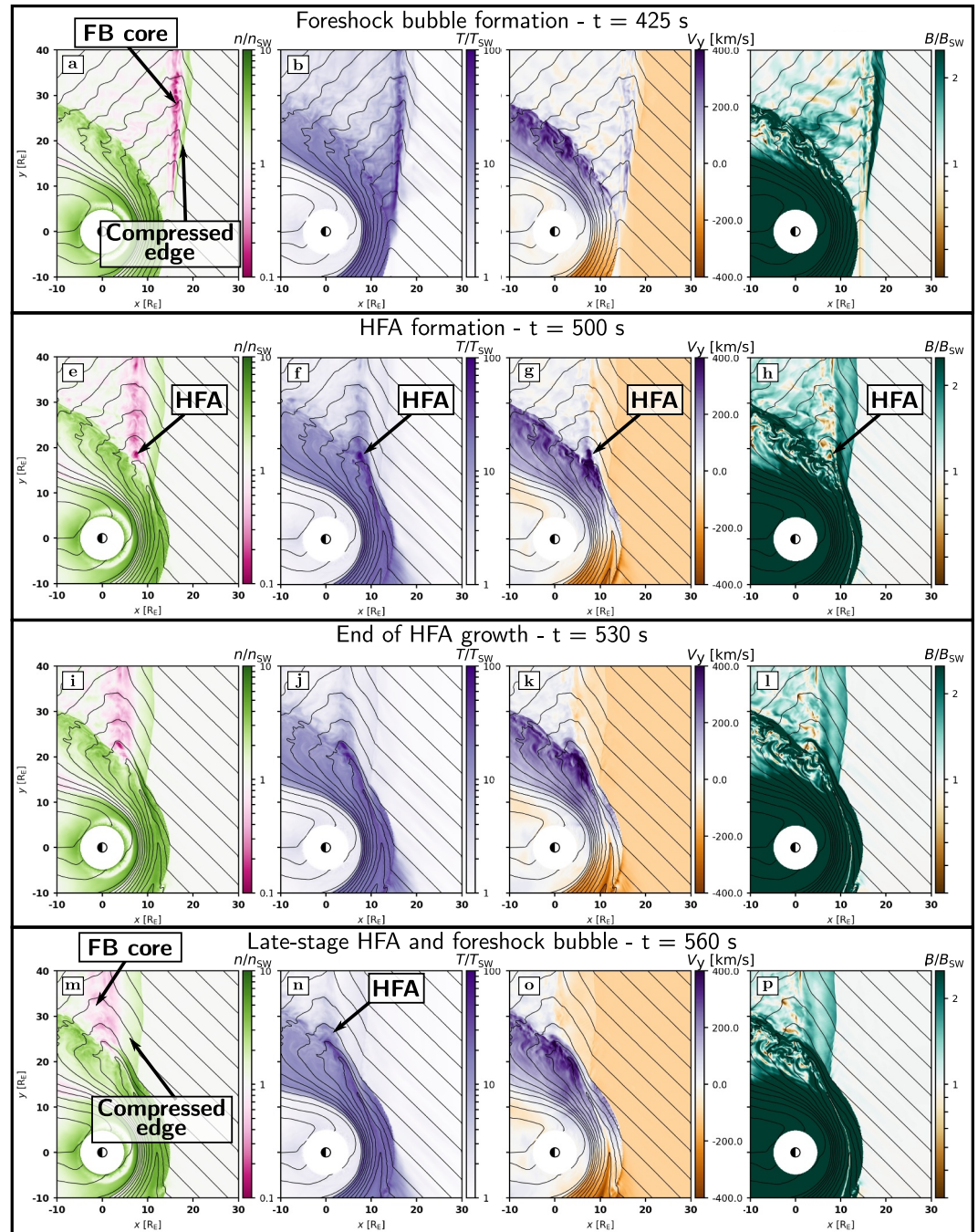


**Figure 1.** Close-ups of the simulation domain illustrating four different stages of the evolution of the foreshock transients. The left column shows the proton density, normalized to the solar wind value, the second column the proton temperature normalized to the solar wind value, the third column the  $y$ -component of the proton bulk velocity and the fourth column the magnetic field strength, normalized to the interplanetary magnetic field strength.

change in parameters initially takes place over one grid cell, but the discontinuity broadens to a couple  $R_E$  thickness as it travels earthward.

### 3. Results

Figure 1 shows an overview of the simulation at four different times. At  $t = 425$  s (top row), the discontinuity has traveled to  $x \sim 14 R_E$ , as shown by the field lines (black lines), but has not yet reached the bow shock. On the

dawn side ( $y < 0$ ) it has retained its narrow structure. On the dusk side, its interaction with foreshock ions has generated a foreshock bubble, characterized by a core with low density, down to 10% of the solar wind values in some places (pink region in Figure 1a), and high temperature, up to  $100 T_{\text{SW}}$  (Figure 1b). This is accompanied by a flow deflection in the dawn-dusk direction (positive  $V_y$  enhancement in Figure 1c). The magnetic field strength is more variable, showing decreases down to 50% of the interplanetary magnetic field (IMF) strength (Figure 1d). This agrees well with spacecraft observations (Turner et al., 2013; Liu et al., 2016). The foreshock bubble core is bounded on its upstream side by a region of compressed plasma and magnetic field with lower temperature (Figures 1a–1d). The structure is elongated, extending over  $\sim 30 R_E$  along the  $y$ -direction, spanning the entire length of the foreshock inside the simulation domain, consistent with foreshock bubble topology described by Omidi, Lee, et al. (2020).

As the rotational discontinuity travels anti-sunward, both the core of the foreshock bubble and its compressed edge expand (Figures 1e–1h), spanning about  $10 R_E$  along the Sun-Earth line at  $t = 500$  s. At this stage, the highest temperatures are found where the discontinuity intersects the quasi-parallel bow shock. These high temperatures are accompanied by strong  $V_y$  enhancements (Figure 1g). This suggests that additional accumulation of suprathermal ions occurs where the discontinuity intersects the bow shock, resulting in the formation of a hot flow anomaly (HFA).

To understand the HFA formation mechanism, the top panels of Figure 2 show the electric field  $x$ -component (a) shortly before the discontinuity reaches the shock, (b) when two HFAs start forming (cyan contours) and (c) when they have merged into a larger structure. A necessary condition for HFA generation is that the motional electric field points toward the discontinuity on at least one side (e.g., Thomsen et al. (1993); Zhao et al. (2017); Zhang et al. (2022)). In our simulation, the unperturbed solar wind motional electric field is directed in the out-of-plane direction on either side of the discontinuity, which should prevent HFA formation. Foreshock waves cause small in-plane electric field oscillations with peak-to-peak amplitudes  $\sim 0.2$  mV/m (see Figure 2a), but their temporal variations likely hamper efficient ion concentration. More importantly,  $E_x$  fluctuations reaching up to  $\sim 1$  mV/m arise inside the foreshock bubble and intensify when approaching the bow shock (Figures 2a–2c).

Figures 2d–2e also show that the foreshock bubble modifies its driving discontinuity, which has evolved into a complex structure with successive field rotations associated with multiple current sheets. The discontinuity's initial current sheet bifurcates, forming one layer of negative current density  $J_z$  on the bubble's earthward side and another at the transition between its core and its compressed sheath, with a positive  $J_z$  current sheet in-between. Similarly, layers of strong currents are visible in  $J_y$  (Figure 2d). As they cross the discontinuity, foreshock ions become demagnetized, creating a Hall current (An et al., 2020; Vu et al., 2022). The emergence of multiple current sheets is likely due to this Hall current and the current driven by solar wind ions as they respond to the field changes caused by the Hall current (Vu et al., 2022).

We note that  $E_x$  converges where  $B_y$  changes sign within the two negative  $J_z$  current sheets (dashed lines in Figures 2a and 2b). Upon reaching the bow shock, each of these two current sheets is associated with a region of enhanced temperature and deflected flows: HFAs (cyan contours in Figure 2b, marking where  $V_y = 350$  km s $^{-1}$  and  $T = 20$  MK). These structures likely form due to foreshock suprathermal ions being channeled toward the discontinuity by the electromagnetic fields (Liu, An, et al., 2020). We checked that the foreshock suprathermal ions retain similar characteristics on the earthward side of the foreshock bubble as in the unperturbed foreshock (not shown), therefore enabling typical HFA formation once favorable electric field orientations emerge. Later, the two HFAs merge into a larger structure (Figure 2c). The current sheets have also further evolved, and only one  $B_y$  rotation is visible at that stage (dashed line in Figure 2c).

Figures 2a–2c display the  $x$ -component of the full electric field. Panels f and i show the contributions of the Hall and convection electric fields separately. The Hall electric field  $E_{\text{Hall}} = \frac{\mathbf{J} \times \mathbf{B}}{n_e e}$  (with the electron density  $n_e = n_{\text{proton}}$  in our simulation and  $e$  the elementary charge) is slightly enhanced at the current sheets mentioned above, and at the foreshock bubble's shock, consistent with the presence of strong currents.  $E_{\text{Hall}_x}$  converges at the same two current sheets as the total  $E_x$  and in some places, it amounts to  $\sim 30\%$  of the total  $E_x$ . The largest part of  $E_x$  is however due to the convection electric field  $\mathbf{E}_{\text{conv}} = -\mathbf{V} \times \mathbf{B}$  (Figure 2i), which arises due to a positive  $V_y$  throughout the foreshock bubble and variations in  $B_z$  (Figures 2g and 2h). The former is caused by the accumulated suprathermal ions, which have a residual positive  $V_y$  from their backstreaming along the initial IMF even

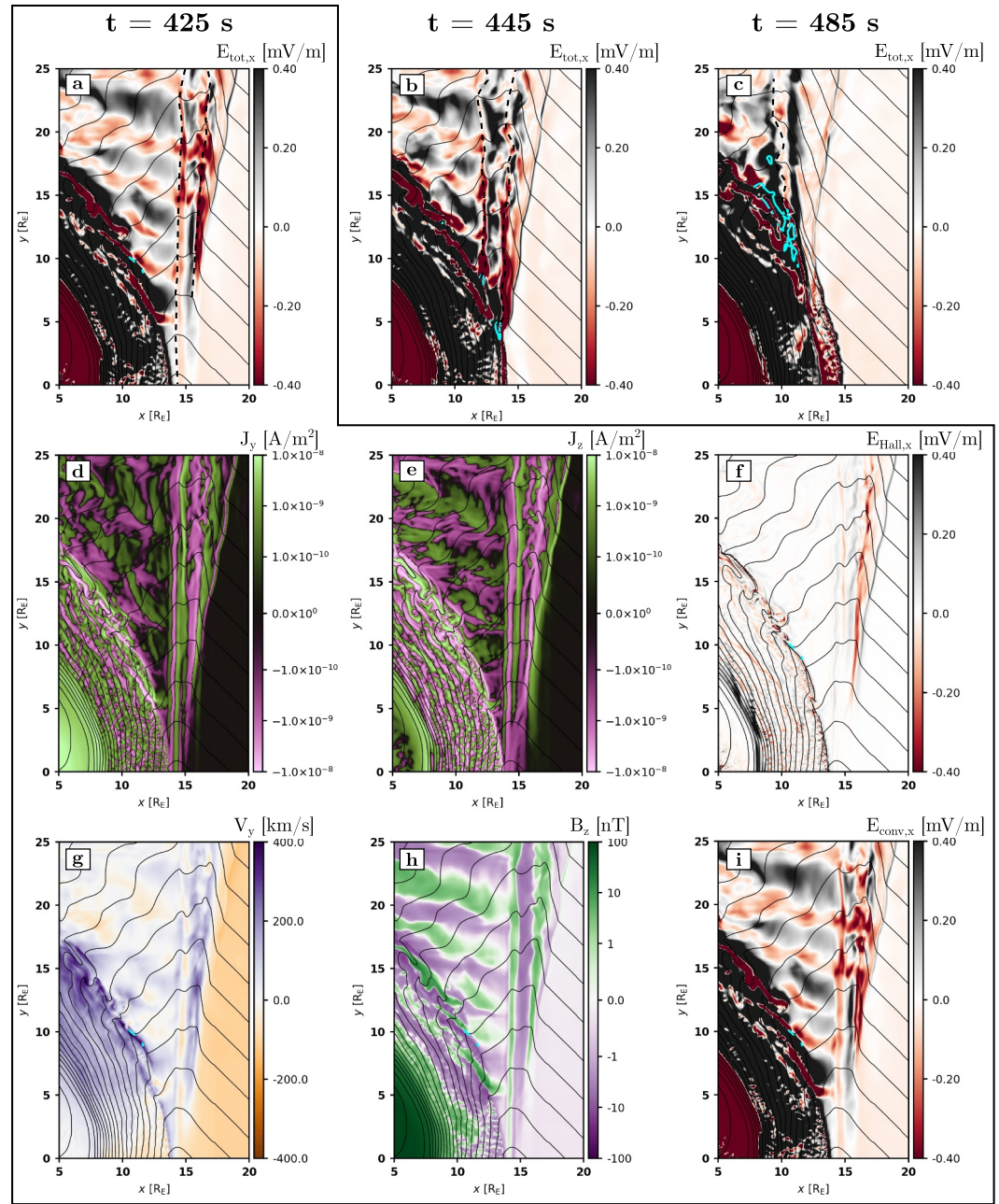


**Figure 2.** (a–c) Color maps of the  $x$ -component of the total electric field  $E_x$  in a close-up on the shock and foreshock bubble, at  $t = 425$  (before the discontinuity reaches the shock), 445 and 485 s. The dashed lines in panels a–c are drawn where  $B_y$  turns from positive to negative within the foreshock bubble. The cyan contours depict where  $V_y = 350 \text{ km s}^{-1}$  and  $T = 20 \text{ MK}$ . The rest of the panels are shown at  $t = 425 \text{ s}$ . (d) and (e)  $y$ - and  $z$ - components of the current density; (f)  $x$ -component of the Hall electric field; (g) Plasma velocity  $V_y$ ; (h) magnetic field  $B_z$  and (i)  $x$ -component of the convection electric  $\mathbf{E}_{\text{conv}} = -\mathbf{V} \times \mathbf{B}$ .

after crossing the discontinuity. The bipolar  $B_z$  signatures are in turn caused by the  $J_y$  currents associated with these ions. This indicates that the foreshock bubble enables HFA generation at the shock.

Once the HFAs form, the strongest deviations in the plasma parameters are observed there, while the foreshock bubble keeps expanding and its signatures become weaker (see Figure 1). The HFA signatures are reinforced as the discontinuity tracks along the bow shock, until about the terminator where they start weakening as well. At  $t = 560 \text{ s}$  (bottom row of Figure 1), the temperature in the core is only  $\sim 10 T_{\text{SW}}$ , down from  $\sim 100 T_{\text{SW}}$  at earlier

times, and the minimum density has re-increased to 25% of the solar wind value. Despite this weakening, the plasma parameters within the transient still strongly deviate from the ambient solar wind.

Finally, we investigate the impact of the foreshock transients on the bow shock. We use two proxies for the shock position, based on local plasma properties, similarly as in Battarbee et al. (2020): (a) shock compression, with a threshold set where the proton density reaches twice the solar wind density, and (b) heating of the solar wind core to three times its initial value (Wilson et al., 2014). These thresholds are depicted with light gray and orange lines in Figure 3. The criterion on the magnetosonic Mach number in Battarbee et al. (2020) is not employed because it requires determining the shock normal direction. Here, the irregular shock shape after the transient's impact, as well as the presence of the foreshock bubble's own shock, prevent us from applying a polynomial fit to calculate the shock normal direction (Battarbee et al., 2020). Before the discontinuity reaches the bow shock (Figure 3a), the two contours are in reasonable agreement with each other, although deviations by up to a couple of Earth radii are visible in some places, consistent with Battarbee et al. (2020). The compressed region sunward of the foreshock bubble is also clearly delineated by a light gray contour in Figures 3a and 3b, but at later times only parts of it reach twice the solar wind density (Figures 3c and 3d), indicating again the structure's weakening.

The impact of the foreshock bubble induces large-scale bow shock deformation (Figures 3b–3d). We identify two main features: a region of low plasma density which penetrates deep into the magnetosheath, and a stripe of hot and compressed plasma protruding outwards into the foreshock. The region with low plasma density is the part of the foreshock bubble's core which has crossed into the magnetosheath. The exact bow shock position is however hard to pinpoint in this area: the density and core heating contours largely deviate from each other, and there is no clear jump in the plasma parameters. This is due to the low Mach number in the bubble's core, where  $M_{ms} \sim 1 - 2$  (Figure 3e), resulting in a localized weakening, or erosion, of the shock. The density contour suggests that this portion of the shock has moved several  $R_E$  earthward. This is however an artifact of its definition using the solar wind density: the plasma in the bubble's core is so tenuous that it does not meet our criterion for plasma compression even after being processed through the shock. Compression is also lower due to the lower  $M_{ms}$ . The orange contour (solar wind heating), on the other hand, suggests that the bow shock is locally bulging out. In panel b, it captures a large part of the foreshock transient core, indicating significant heating of the solar wind core in this region. At later times, the orange contour may be closer to the actual shock position. However, the ion velocity distribution functions just inwards of the orange contour at  $t = 550$  s (not shown) reveal that the plasma is not slowed down, suggesting that part of this area is still upstream of the shock. The shock transition lies somewhere in-between these two contours. Just sunward of its eroded portion, the bow shock expands outwards into the foreshock bubble's compressed edge (Figures 3b and 3c). This expansion could be due to the change in  $M_{ms}$ , which is  $\sim 3 - 4$  in the bubble's sheath, higher than in its core but still significantly lower than in the pristine solar wind (Figures 3e and 3f).

#### 4. Discussion and Conclusions

This study shows that both a foreshock bubble and an HFA, or rather multiple HFAs which later merge, can form along the same rotational discontinuity. The emergence of multiple transients at a single discontinuity has been previously reported in simulations by Omidi, Collinson, and Sibeck (2020) and Omidi, Lee, et al. (2020). Similarly as in our run, there is no electric field component pointing toward the discontinuity in the initial conditions used in these works. The mechanism we propose here likely also applies in these simulations. Different IMF orientations before and after the discontinuity, as well as different discontinuity normal directions, were used in each case, indicating that this is not due to a very specific geometry, but could be a common occurrence. Furthermore, the work by Omidi, Collinson, and Sibeck (2020) was based on a 3D simulation, thus ruling out that the HFA formation could be an artifact of our 2D geometry.

We found that the HFA generation is enabled by the foreshock bubble itself. As in Omidi, Collinson, and Sibeck (2020), we noted that the discontinuity broadens into a more complex structure and that two HFAs form where two field rotations reach the bow shock. We showed that the electric field converges in these two current sheets due to foreshock ion-driven currents, creating a positive feedback loop allowing further suprathermal ion concentration. The converging electric fields are dominated by the convection electric field, but the Hall field is non-negligible and likely contributes to the HFA growth also. It is however possible that for other discontinuity orientations, HFA formation may instead be suppressed, as shown in Vu et al. (2024).

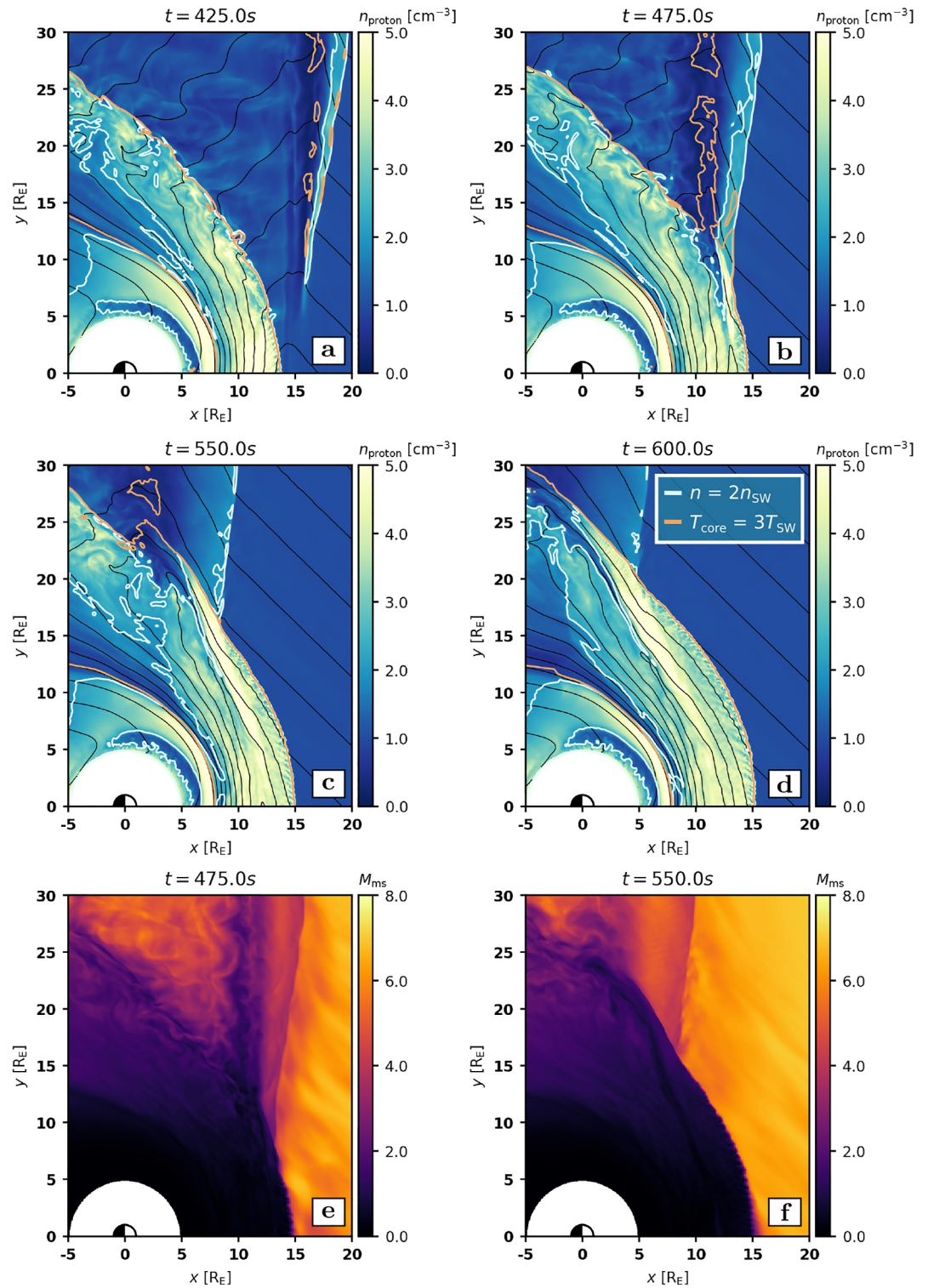


**Figure 3.** Close-up of the impact of the foreshock transient on the bow shock. (a–d) Proton density at four different times in the simulation. The colored contours are proxies of the shock position: proton density reaching twice the solar wind density (light gray) and core temperature reaching three times the solar wind temperature (orange). (e) and (f) magnetosonic Mach number at  $t = 475$  and  $550$  s.

Once the discontinuity reaches the bow shock and the HFAs start growing, the strongest deviations of the plasma parameters are found within the HFAs, consistent with Omid, Lee, et al. (2020). This is not only due to the HFAs forming, but also to the foreshock bubble signatures weakening from that time onwards in the simulation. This evolution corresponds to the remission stage in the two-phase scenario proposed by Liu et al. (2016) based on multi-point observations. After the initial growth stage, the expansion of the foreshock bubble continues, but the concentrated foreshock ions do not provide enough energy anymore to sustain the acceleration of all the solar wind plasma to the foreshock bubble's sheath flow speed (in the solar wind frame) (Liu et al., 2016). The expansion energy is provided by the kinetic energy of the foreshock ions. The kinetic energy density is largest at the sunward edge of the foreshock, because of the larger Mach number closer to the bow shock nose and because the field-aligned beams are faster closer to the foreshock edge (Kempf et al., 2015). When the discontinuity has reached the bow shock, the suprathermal ions which then sustain the foreshock bubble have a lower kinetic energy density. Also, part of the energy is then transferred to HFA growth. This likely explains why the structure transitions to its remission stage at this point.

Previous works have shown that foreshock transients can survive far into the nightside (Wang et al., 2018; Wang et al., 2020; T. Z. Liu, Wang, et al., 2020; Liu et al., 2021). While our simulation box does not include the magnetotail, we note that the foreshock bubble properties at the downstream edge of the domain still depart strongly from those in the ambient solar wind and foreshock. A similar evolution is observed in the 3D simulation by Wang et al. (2020) including the magnetotail: the foreshock bubble keeps expanding as it travels downtail, while the temperature in its core decreases after an initial enhancement (see Figure 2 in Wang et al. (2020)). This supports the fact that foreshock transient properties keep evolving as they travel antisunward, and even though their signatures may start decaying early on, they retain their distinguishable features.

Omid, Lee, et al. (2020) have suggested that the bow shock and the foreshock bubble compressed edge can combine into a single structure at large IMF cone angles. Here, a similar phenomenon takes place at first when the foreshock bubble edge interacts with the subsolar bow shock, but rapidly, the actual shock is found in-between the nominal bow shock position and the foreshock bubble's shock. This difference with the study by Omid, Lee, et al. (2020) is likely due to the lower cone angle in our simulation ( $45^\circ$  compared to  $60^\circ$ ). Identifying the exact shock position is challenging, as plasma heating and density depletion associated with the foreshock transients lead to the shock position proxies disagreeing to a significant degree, suggesting that additional criteria or more detailed cross-evaluation of those suggested in Battarbee et al. (2020) is required in these circumstances.

MHD simulations show that the impact of a low density solar wind slab causes the shock to bulge out locally, creating HFA-like signatures at/downstream of the shock (Lu et al., 2024; Sibeck et al., 2025). The same MHD mechanisms are likely operating in our simulation, contributing to the  $V_y$  and temperature enhancements downstream of the shock (Figures 1j and 1k and 1n-1o). However, the formation of multiple HFAs in our simulation, associated with upstream current sheets, indicates that kinetic processes are at play. Disentangling the relative contributions of these mechanisms is left for future work.

Since the foreshock transients develop on the flank in our simulation, their geoeffectiveness is limited. If they formed in the subsolar region, the foreshock bubble-driven HFAs could reinforce the impact of the foreshock bubble, in creating stronger dynamic pressure variations. In some geometries, the HFAs and the foreshock bubble may also separate, as foreshock bubbles move at the solar wind speed while HFAs propagate with their driving discontinuity (Turner et al., 2013). This could result in more global geo-effects, to be investigated in other simulations.

Finally, our results regarding the formation of different types of transients at a single discontinuity imply that depending on the position of an observing spacecraft, one may reach different conclusions on its nature. Multi-point observations of foreshock transients with large enough spacecraft separation would provide crucial information on the formation and interplay between these multiple transients. Our simulation suggests that spacecraft separations of a few  $R_E$  are required to probe simultaneously the foreshock bubble and the HFA. Observations by THEMIS in 2008–2009 and Cluster in 2018–2019 provide suitable separations and could be revisited to search for candidate events. Measurements near the shock should be complemented with upstream solar wind data to assess whether the electric field was pointing toward the discontinuity prior to the foreshock bubble formation, as otherwise the HFA properties will be similar regardless of their formation mechanism.

## Data Availability Statement

Vlasiator (Pfau-Kempf et al., 2021) is distributed under the GPL-2 open-source license. Vlasiator uses a data structure developed in-house. The Analysator software (Battarbee et al., 2021) was used to produce the presented figures. The run described here can be either run with the above-mentioned code using the boundary conditions reported in this paper, or the data sets can be downloaded from the University of Helsinki servers where they are stored (Suni & Pfau-Kempf, 2025).

## Acknowledgments

The work of LT, SD, ST and VL is funded by the European Union (ERC Grant WAVESTORMS–101124500). Views and opinions expressed are however those of the author(s) only and do not necessarily reflect those of the European Union or the European Research Council Executive Agency. Neither the European Union nor the granting authority can be held responsible for them. This work was supported by the International Space Science Institute (ISSI) in Bern, through ISSI International Team project #555. We acknowledge fruitful discussions with the other members of ISSI team #555, in particular Nick Omidi, Yu Lin and David Sibeck. We acknowledge the CSC–IT Center for Science computational project 2004873 (WAVESTORMS), with which the simulation run used in this study was produced. MOA was supported by UKRI (STFC/EPSRC) Stephen Hawking Fellowship EP/T01735X/1 and UKRI Future Leaders Fellowship MR/X034704/1. The work of JS was made possible by a doctoral researcher position at the Doctoral Programme in Particle Physics and Universe Sciences funded by the University of Helsinki. PK's work was funded by the DGAPA PAPIIT IN100424 Grant. YP acknowledges the Research Council of Finland Grant 339756 (KIMCHI). MP and MB acknowledge the Finnish Centre of Excellence in Research of Sustainable Space, funded through the Research Council of Finland Grants 312351, 336805, and 352846. MP additionally acknowledges the Research Council of Finland Grant 361901. SR acknowledges support from Johns Hopkins University Applied Physics Laboratory independent R&D fund. XBC is thankful for DGAPA PAPIIT IN106724 and CONAHCyT CBF2023–2024–852 Grants. Open access publishing facilitated by Helsingin yliopisto, as part of the Wiley - FinELib agreement.

## References

- An, X., Liu, T. Z., Bortnik, J., Osmane, A., & Angelopoulos, V. (2020). Formation of foreshock transients and associated secondary shocks. *The Astrophysical Journal*, *901*(1), 73. <https://doi.org/10.3847/1538-4357/abaf03>
- Archer, M. O., Turner, D. L., Eastwood, J. P., Schwartz, S. J., & Horbury, T. S. (2015). Global impacts of a Foreshock Bubble: Magnetosheath, magnetopause and ground-based observations. *Planetary and Space Science*, *106*, 56–66. <https://doi.org/10.1016/j.pss.2014.11.026>
- Battarbee, M., Ganse, U., Pfau-Kempf, Y., Turc, L., Brito, T., Grandin, M., et al. (2020). Non-locality of Earth's quasi-parallel bow shock: Injection of thermal protons in a hybrid-Vlasov simulation. *Annales Geophysicae*, *38*(3), 625–643. <https://doi.org/10.5194/angeo-38-625-2020>
- Battarbee, M., Hannuksela, O. A., Pfau-Kempf, Y., Alfthan, S. V., Ganse, U., Jarvinen, R., et al. (2021). Fmihipc/analysator: V0.9 [Software]. Zenodo. <https://doi.org/10.5281/ZENODO.4462515>
- Blanco-Cano, X., Battarbee, M., Turc, L., Dimmock, A. P., Kilpua, E. K. J., Hoilijoki, S., et al. (2018). Cavitons and spontaneous hot flow anomalies in a hybrid-Vlasov global magnetospheric simulation. *Annales Geophysicae*, *36*(4), 1081–1097. <https://doi.org/10.5194/angeo-36-1081-2018>
- Blanco-Cano, X., Omidi, N., & Russell, C. T. (2009). Global hybrid simulations: Foreshock waves and cavitons under radial interplanetary magnetic field geometry. *Journal of Geophysical Research (Space Physics)*, *114*(A1), A01216. <https://doi.org/10.1029/2008JA013406>
- Eastwood, J. P., Lucek, E. A., Mazelle, C., Meziane, K., Narita, Y., Pickett, J., & Treumann, R. A. (2005). The foreshock. *Space Science Reviews*, *118*(1–4), 41–94. <https://doi.org/10.1007/s11214-005-3824-3>
- Ganse, U., Koskela, T., Battarbee, M., Pfau-Kempf, Y., Papadakis, K., Alho, M., et al. (2023). Enabling technology for global 3D + 3V hybrid-Vlasov simulations of near-Earth space. *Physics of Plasmas*, *30*(4), 042902. <https://doi.org/10.1063/5.0134387>
- Kajdič, P., Blanco-Cano, X., Turc, L., Archer, M., Raptis, S., Liu, T. Z., et al. (2024). Transient upstream mesoscale structures: Drivers of solar-quiet space weather. *Frontiers in Astronomy and Space Sciences*, *11*, 1436916. <https://doi.org/10.3389/fspas.2024.1436916>
- Kempf, Y., Pokhotelov, D., Gutynska, O., Wilson, L. B., III, Walsh, B. M., von Alfthan, S., et al. (2015). Ion distributions in the Earth's foreshock: Hybrid-Vlasov simulation and THEMIS observations. *Journal of Geophysical Research (Space Physics)*, *120*(5), 3684–3701. <https://doi.org/10.1002/2014JA020519>
- Lin, Y. (1997). Generation of anomalous flows near the bow shock by its interaction with interplanetary discontinuities. *Journal of Geophysical Research*, *102*(A11), 24265–24282. <https://doi.org/10.1029/97JA01989>
- Liu, T. Z., An, X., Zhang, H., & Turner, D. (2020a). Magnetospheric multiscale observations of foreshock transients at their very early stage. *The Astrophysical Journal*, *902*(1), 5. <https://doi.org/10.3847/1538-4357/abb249>
- Liu, T. Z., Angelopoulos, V., & Lu, S. (2019). Relativistic electrons generated at Earth's quasi-parallel bow shock. *Science Advances*, *5*(7), eaaw1368. <https://doi.org/10.1126/sciadv.aaw1368>
- Liu, T. Z., Turner, D. L., Angelopoulos, V., & Omidi, N. (2016). Multipoint observations of the structure and evolution of foreshock bubbles and their relation to hot flow anomalies. *Journal of Geophysical Research (Space Physics)*, *121*(6), 5489–5509. <https://doi.org/10.1002/2016JA022461>
- Liu, T. Z., Wang, C.-P., Wang, B., Wang, X., Zhang, H., Lin, Y., & Angelopoulos, V. (2020b). ARTEMIS observations of foreshock transients in the midtail foreshock. *Geophysical Research Letters*, *47*(21), e90393. <https://doi.org/10.1029/2020GL090393>
- Liu, T. Z., Zhang, H., Wang, C.-P., Angelopoulos, V., Vu, A., Wang, X., & Lin, Y. (2021). Statistical study of foreshock transients in the midtail foreshock. *Journal of Geophysical Research (Space Physics)*, *126*(5), e29156. <https://doi.org/10.1029/2021JA029156>
- Liu, Z., Turner, D. L., Angelopoulos, V., & Omidi, N. (2015). THEMIS observations of tangential discontinuity-driven foreshock bubbles. *Geophysical Research Letters*, *42*(19), 7860–7866. <https://doi.org/10.1002/2015GL065842>
- Lu, X., Otto, A., Zhang, H., Liu, T., & Chen, X. (2024). The bow shock and magnetosheath responses to density depletion structures. *Journal of Geophysical Research (Space Physics)*, *129*(5), e2024JA032566. <https://doi.org/10.1029/2024JA032566>
- Omidi, N., Collinson, G., & Sibeck, D. (2020a). Foreshock bubbles at Venus: Hybrid simulations and VEX observations. *Journal of Geophysical Research (Space Physics)*, *125*(2), e27056. <https://doi.org/10.1029/2019JA027056>
- Omidi, N., Eastwood, J. P., & Sibeck, D. G. (2010). Foreshock bubbles and their global magnetospheric impacts. *Journal of Geophysical Research (Space Physics)*, *115*(A6), A06204. <https://doi.org/10.1029/2009JA014828>
- Omidi, N., Lee, S. H., Sibeck, D. G., Turner, D. L., Liu, T. Z., & Angelopoulos, V. (2020b). Formation and topology of foreshock bubbles. *Journal of Geophysical Research (Space Physics)*, *125*(9), e28058. <https://doi.org/10.1029/2020JA028058>
- Palmroth, M., Archer, M., Vainio, R., Hietala, H., Pfau-Kempf, Y., Hoilijoki, S., et al. (2015). ULF foreshock under radial IMF: THEMIS observations and global kinetic simulation Vlasiator results compared. *Journal of Geophysical Research: Space Physics*, *120*(10), 8782–8798. <https://doi.org/10.1002/2015JA021526>
- Palmroth, M., Ganse, U., Pfau-Kempf, Y., Battarbee, M., Turc, L., Brito, T., et al. (2018). Vlasov methods in space physics and astrophysics. *Living Reviews in Computational Astrophysics*, *4*, 1. <https://doi.org/10.1007/s41115-018-0003-2>
- Pfau-Kempf, Y., Battarbee, M., Ganse, U., Hoilijoki, S., Turc, L., von Alfthan, S., et al. (2018). On the importance of spatial and velocity resolution in the hybrid-Vlasov modeling of collisionless shocks. *Frontiers in Physics*, *6*, 44. <https://doi.org/10.3389/fphy.2018.00044>
- Pfau-Kempf, Y., Von Alfthan, S., Sandroos, A., Ganse, U., Koskela, T., Battarbee, M., et al. (2021). Fmihipc/vlasiator: Vlasiator 5.1 [Software]. Zenodo. <https://doi.org/10.5281/ZENODO.4719554>
- Raptis, S., Lalti, A., Lindberg, M., Turner, D. L., Caprioli, D., & Burch, J. L. (2025). Revealing an unexpectedly low electron injection threshold via reinforced shock acceleration. *Nature Communications*, *16*(1), 488. <https://doi.org/10.1038/s41467-024-55641-9>
- Schwartz, S. J. (1995). Hot flow anomalies near the Earth's bow shock. *Advances in Space Research*, *15*(8–9), 107–116. [https://doi.org/10.1016/0273-1177\(94\)00092-F](https://doi.org/10.1016/0273-1177(94)00092-F)
- Schwartz, S. J., Chaloner, C. P., Christiansen, P. J., Coates, A. J., Hall, D. S., Johnstone, A. D., et al. (1985). An active current sheet in the solar wind. *Nature*, *318*(6043), 269–271. <https://doi.org/10.1038/318269a0>

- Schwartz, S. J., Paschmann, G., Sckopke, N., Bauer, T. M., Dunlop, M., Fazakerley, A. N., & Thomsen, M. F. (2000). Conditions for the formation of hot flow anomalies at Earth's bow shock. *Journal of Geophysical Research*, *105*(A6), 12639–12650. <https://doi.org/10.1029/1999JA000320>
- Sibeck, D. G., Rastätter, L., & El Alaoui, M. (2025). Using a magnetohydrodynamic (MHD) model to simulate the magnetospheric response to a kinetic foreshock transient. *Geophysical Research Letters*, *52*(5), 2024GL113463. <https://doi.org/10.1029/2024GL113463>
- Suni, J., & Pfau-Kempf, Y. (2025). Vlasior simulation data (run AIC). [Dataset]. *Geoscientific Model Development*. <http://urn.fi/urn:nbn:fi:fd-361c3d4f-7d4f-3bc4-98cd-d7a22d0b8127>
- Tarvus, V., Turc, L., Battarbee, M., Suni, J., Blanco-Cano, X., Ganse, U., et al. (2021). Foreshock cavitons and spontaneous hot flow anomalies: A statistical study with a global hybrid-Vlasov simulation. *Annales Geophysicae*, *39*(5), 911–928. <https://doi.org/10.5194/angeo-39-911-2021>
- Thomsen, M. F., Thomas, V. A., Winske, D., Gosling, J. T., Farris, M. H., & Russell, C. T. (1993). Observational test of hot flow anomaly formation by the interaction of a magnetic discontinuity with the bow shock. *Journal of Geophysical Research*, *98*(A9), 15319–15330. <https://doi.org/10.1029/93JA00792>
- Turc, L., Ganse, U., Pfau-Kempf, Y., Hoilijoki, S., Battarbee, M., Juusola, L., et al. (2018). Foreshock properties at typical and enhanced interplanetary magnetic field strengths: Results from hybrid-Vlasov simulations. *Journal of Geophysical Research: Space Physics*, *123*(7), 5476–5493. <https://doi.org/10.1029/2018JA025466>
- Turc, L., Roberts, O. W., Archer, M. O., Palmroth, M., Battarbee, M., Brito, T., et al. (2019). First observations of the disruption of the Earth's foreshock wave field during magnetic clouds. *Geophysical Research Letters*, *46*(22), 12644–12653. <https://doi.org/10.1029/2019GL084437>
- Turc, L., Roberts, O. W., Verscharen, D., Dimmock, A. P., Kajdič, P., Palmroth, M., et al. (2023). Transmission of foreshock waves through Earth's bow shock. *Nature Physics*, *19*(1), 78–86. <https://doi.org/10.1038/s41567-022-01837-z>
- Turner, D. L., Omid, N., Sibeck, D. G., & Angelopoulos, V. (2013). First observations of foreshock bubbles upstream of Earth's bow shock: Characteristics and comparisons to HFAs. *Journal of Geophysical Research (Space Physics)*, *118*(4), 1552–1570. <https://doi.org/10.1002/jgra.50198>
- Turner, D. L., Wilson, L. B., Liu, T. Z., Cohen, I. J., Schwartz, S. J., Osmane, A., et al. (2018). Autogenous and efficient acceleration of energetic ions upstream of Earth's bow shock. *Nature*, *561*(7722), 206–210. <https://doi.org/10.1038/s41586-018-0472-9>
- Valek, P. W., Thomsen, M. F., Allegrini, F., Bagenal, F., Bolton, S., Connerney, J., et al. (2017). Hot flow anomaly observed at Jupiter's bow shock. *Geophysical Research Letters*, *44*(16), 8107–8112. <https://doi.org/10.1002/2017GL073175>
- Vu, A., Liu, T. Z., Angelopoulos, V., & Zhang, H. (2024). 2.5-D local hybrid simulations of discontinuity-driven compressional boundaries under various magnetic field geometries. *Journal of Geophysical Research (Space Physics)*, *129*(5), e2023JA032302. <https://doi.org/10.1029/2023JA032302>
- Vu, A., Liu, T. Z., Zhang, H., & Delamere, P. (2022). Hybrid simulations of a tangential discontinuity-driven foreshock bubble formation in comparison with a hot flow anomaly formation. *Journal of Geophysical Research (Space Physics)*, *127*(6), e29973. <https://doi.org/10.1029/2021JA029973>
- Wang, C.-P., Liu, T. Z., Xing, X., & Masson, A. (2018). Multispacecraft observations of tailward propagation of transient foreshock perturbations to midtail magnetosheath. *Journal of Geophysical Research (Space Physics)*, *123*(11), 9381–9394. <https://doi.org/10.1029/2018JA025921>
- Wang, C.-P., Wang, X., Liu, T. Z., & Lin, Y. (2020). Evolution of a foreshock bubble in the midtail foreshock and impact on the magnetopause: 3-D global hybrid simulation. *Geophysical Research Letters*, *47*(22), e89844. <https://doi.org/10.1029/2020GL089844>
- Wang, C.-P., Wang, X., Liu, T. Z., & Lin, Y. (2021). A foreshock bubble driven by an IMF tangential discontinuity: 3D global hybrid simulation. *Geophysical Research Letters*, *48*(9), e93068. <https://doi.org/10.1029/2021GL093068>
- Wilson, L. B. (2016). Low frequency waves at and upstream of collisionless shocks. *Washington DC American Geophysical Union Geophysical Monograph Series*, *216*, 269–291. <https://doi.org/10.1002/9781119055006.ch16>
- Wilson, L. B., Sibeck, D. G., Breneman, A. W., Le Contel, O., Cully, C., Turner, D. L., et al. (2014). Quantified energy dissipation rates in the terrestrial bow shock: 1. Analysis techniques and methodology. *Journal of Geophysical Research (Space Physics)*, *119*(8), 6455–6474. <https://doi.org/10.1002/2014JA019929>
- Wilson, L. B., Sibeck, D. G., Turner, D. L., Osmane, A., Caprioli, D., & Angelopoulos, V. (2016). Relativistic electrons produced by foreshock disturbances observed upstream of Earth's bow shock. *Physical Review Letters*, *117*(21), 215101. <https://doi.org/10.1103/PhysRevLett.117.215101>
- Zhang, H., Zong, Q., Connor, H., Delamere, P., Facskó, G., Han, D., et al. (2022). Dayside transient phenomena and their impact on the magnetosphere and ionosphere. *Space Science Reviews*, *218*(5), 40. <https://doi.org/10.1007/s11214-021-00865-0>
- Zhao, L. L., Zhang, H., & Zong, Q. G. (2017). A statistical study on hot flow anomaly current sheets. *Journal of Geophysical Research (Space Physics)*, *122*(1), 235–248. <https://doi.org/10.1002/2016JA023319>